JOURNAL OF MATERIALS SCIENCE **41** (2006) 107–116

Piezoresponse force microscopy and recent advances in nanoscale studies of ferroelectrics

A. GRUVERMAN
North Carolina State University, Raleigh, NC 27695-7920
E-mail: Alexei_Gruverman@ncsu.edu

S. V. KALININ
Oak Ridge National Laboratory, Oak Ridge, Tennessee 37831

In this paper, we review recent advances in piezoresponse force microscopy (PFM) with respect to nanoscale ferroelectric research, summarize the basic principles of PFM, illustrate what information can be obtained from PFM experiments and delineate the limitations of PFM signal interpretation relevant to quantitative imaging of a broad range of piezoelectrically active materials. Particular attention is given to orientational PFM imaging and data interpretation as well as to electromechanics and kinetics of nanoscale ferroelectric switching in PFM.

1. Introduction

Rapid development of electronic devices based on ferroelectric thin films has necessitated studies of ferroelectric properties at the nanoscale. Fortunately, this need came at the time when new techniques for nanoscale characterization of materials became available. Scanning probe microscopy (SPM) has emerged as a powerful tool for high-resolution characterization of virtually all types of materials, including metals, semiconductors, dielectrics, polymers and biomolecules. A number of papers and books on scanning probe methods have been published, providing an introduction to the basic SPM principles and advanced applications [1–5]. SPM techniques have revolutionized the field of ferroelectricity, for the first time providing an opportunity for nondestructive visualization of domain structures in ferroelectric thin films at the nanoscale. SPM made possible nanoscale mapping of the surface potential, evaluation of local electromechanical properties and nonlinear dielectric constant measurements, i.e. it provides crucial information on the ferroelectric materials properties with unprecedented spatial resolution. SPM has also opened new venues in nanoscale domain patterning for such applications as high-density data storage [6, 7] and ferroelectric lithography [8, 9]. Steadily increasing number of research papers indicates a growing importance of SPM in the field of ferroelectricity (Fig. 1). Research groups in US, Europe and Asia are actively using SPM for high-resolution characterization of ferroelectric materials both in bulk and thin layer forms [10].

Among the SPM techniques for the nanoscale characterization of ferroelectrics, by far the most popular one is piezoresponse force microscopy (PFM) [6–10]. In this paper, we review recent advances in PFM with respect to nanoscale ferroelectric research, summarize the basic principles of PFM, illustrate what information can be obtained from PFM experiments and delineate the limitations of PFM signal interpretation relevant to quantitative imaging of a broad range of piezoelectrically active materials.

2. Principle of piezoresponse force microscopy

Piezoresponse force microscopy is based on the detection of local piezoelectric deformation of a ferroelectric sample induced by an external electric field (hence the name "piezoresponse"). Depending on the relative orientations of the applied field and the polarization vector, sample deformation can be in the form of elongation, contraction or shear. For the converse piezoelectric effect, the field-induced strain S_j can be expressed as [11]:

$$S_j = d_{ij}E_i \tag{1}$$

where d_{ij} are components of the piezoelectric tensor (in reduced Voigt notation) and E_i is the applied field.

0022-2461
DOI: 10.1007/s10853-005-5946-0

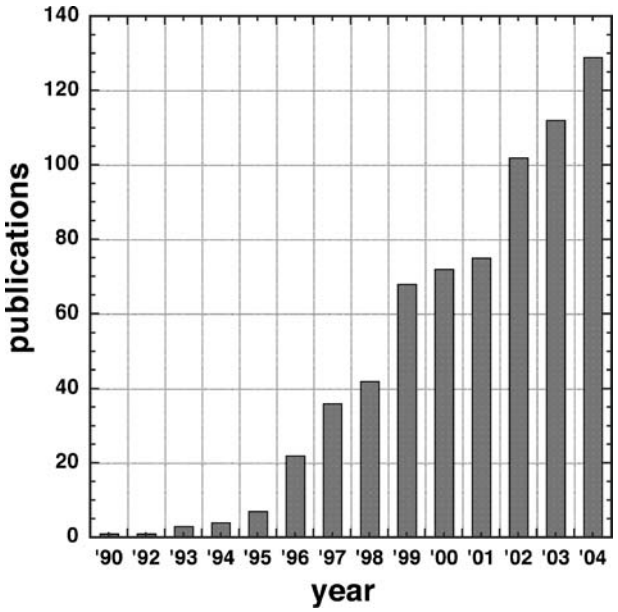

Figure 1 Number of publications on SPM studies of ferroelectrics per year.

Using the thermodynamic approach it can be shown that in a single-domain ferroelectric the piezoelectric coefficient relates to the spontaneous polarization P_s via the following expression [12, 13]:

$$d_{ij} = \varepsilon_{im} Q_{jmk} P_{sk}, \tag{2}$$

where ε_{im} is the dielectric constant and Q_{jmk} is the electrostriction coefficient.

The linear coupling between the piezoelectric and ferroelectric parameters infers that the domain polarity can be determined from the sign of the field-induced strain. Application of the uniform electric field along the polar direction results in the elongation of the domain with polarization parallel to the applied field and in the contraction of the domain with opposite polarization. The field-induced strain in this case can be written as:

$$S = \frac{\Delta Z}{Z} = \pm d_{33} E \tag{3}$$

where ΔZ is the sample deformation and Z is the sample thickness. Equation 3 can be rewritten as:

$$\Delta Z = \pm d_{33} V \tag{4}$$

where V is an applied voltage. The $\pm$ sign reflects the piezoelectric coefficients of opposite sign for antiparallel domains. Thus, opposite domains can be visualized by monitoring their voltage-induced surface displacement.

Due to its extremely high vertical sensitivity, nanoscale topography variations can be routinely measured in SPM. However, domain imaging based on detection of static piezoelectric deformation is difficult to implement unless a sample has a very smooth surface. The reason is simple: the static cantilever deflection due to the piezoelectric deformation will be superimposed on the deflection signal due to the surface roughness, which renders static piezoresponse domain imaging in samples with rough surfaces highly problematical.

Based on Equation 4 one might conclude that the electrically induced topographic contrast between opposite domains can be infinitely enhanced by increasing the imaging voltage. However, there is a strict limitation imposed on this parameter: to perform *nondestructive* visualization of domain structure, the imaging voltage should be kept below the coercive voltage of the ferroelectric sample. In addition, a high imaging voltage will lead to an increased contribution of the electrostatic signal to the tip-sample interaction, which in some cases can obscure the domain image. Given that a typical value of the coercive field in a 200-nm-thick Pb(Zr, Ti)O3 ferroelectric film is approximately 50 kV/cm, the imaging voltage should not exceed 1 V, otherwise the imaging process will change the domain structure by inducing the polarization reversal. In a PZT film with the d_{33} constant of about 200 pm/N the surface displacement induced by an external voltage of 1 V will be only 0.2 nm. Obviously, such a displacement could not be reliably detected in ferroelectric films, where topographic features can be on the order of several nanometers. The static approach can be applied in some limited cases, for example, to ferroelectric samples with carefully polished surfaces, relatively high values of piezoelectric constants and coercive fields.

A problem of low sensitivity of a static piezoresponse mode has been circumvented by employing a dynamic piezoresponse imaging method based on the voltage-modulation approach, which allowed sensitivity to be increased by three orders of magnitude [14–17]. In this approach, an ac modulation (imaging) voltage $V = V_0 \cos \omega t$ is applied to the ferroelectric sample and surface displacement is measured using a standard lock-in technique by detecting the vertical vibration of the cantilever (Fig. 2a), which follows sample surface oscillation. A domain map can be obtained by scanning the surface while detecting the first harmonic component of the normal surface vibration (vertical piezoresponse, or VPFM):

$$\Delta Z = \Delta Z_0 \cos(\omega t + \varphi) \tag{5}$$

where $\Delta Z_0 = d_v V_0$ is a vibration amplitude, d_v is effective piezoelectric constant and φ is a phase difference between the imaging voltage and piezoresponse, which provides information on the polarization direction. With the modulation voltage applied to the probing tip, positive domains (polarization vector oriented downward) will vibrate in phase with the applied voltage so that $\varphi(+) = 0^\circ$, while vibration of negative domains (polarization vector oriented upward) will occur in counter phase: $\varphi(-) =$

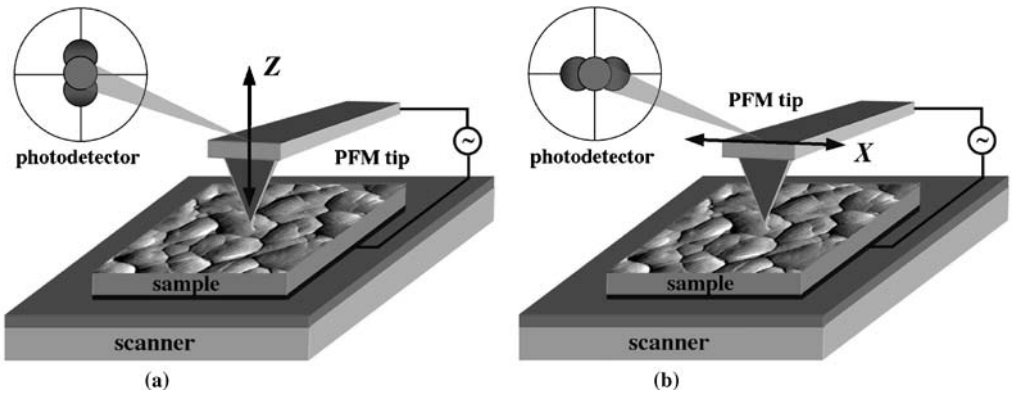

Figure 2 Schematics of the vertical (a) and lateral (b) PFM signal detection.

180°. Note that while Equation 4 is rigorous for a uniform field case, the field below the SPM tip is highly non-uniform. The rigorous solution of this problem has been given by Kalinin and Karapetian [18, 19] and it was shown that for transversally isotropic materials (e.g. *c* domain in tetragonal perovskite ferroelectrics, poled polymers, etc.) $d_v \approx d_{33}$, recovering the early assumptions in PFM data interpretation [16].

It should be noted that despite apparent simplicity of the PFM method, quantification of the PFM data, particularly in the case of thin films, is nontrivial due to the complexity of the tip-sample interaction which involves not only electromechanical but also electrostatic components. Experimental conditions, such as driving voltage, frequency, loading force, cantilever force constant, tip apex radius, ambient environment, as well as physical properties of the samples (thickness, dielectric constants, orientation, defect structure, crystallinity, electrode material) should be taken into account to avoid misinterpretation of the PFM results [20]. However, qualitative PFM domain imaging is extremely robust and currently PFM is one of the main tools for high-resolution characterization of ferroelectric crystals and thin films [21].

One of the significant features of the dynamic PFM method is that it also allows delineation of domains with polarization parallel to the sample surface (*a*-domains) [22–24]. In lateral PFM (LPFM) [22], *a*-domains are visualized by detecting the torsional vibration of the cantilever (Fig. 2b). Application of the modulation voltage across the sample generates sample vibration in the direction parallel to its surface due to the piezoelectric shear deformation. This surface vibration, translated via the friction forces to the torsional movement of the cantilever, can be detected in the same way as the normal cantilever oscillation in vertical PFM. For the uniform field for *a* domain, the amplitude of the in-plane oscillation is given by:

$$\Delta X_0 = d_{15} V_0 \tag{6}$$

while polarization direction can be determined from the phase signal since oscillation phases of opposite *a*-domains differ by 180°. It should be noted, however, that quantification of the shear piezoelectric coefficients in LPFM is a challenging problem that is complicated by the tip-surface tribology, inhomogeneous field distribution and mechanical clamping effects.

Note that Equation 6 can be used only when the in-plane polarization vector is perpendicular to the physical axis of the cantilever. However, in general case the in-plane electromechanical response vector can be oriented arbitrarily with respect to the cantilever. To perform complete three-dimensional (3D) reconstruction of polarization, an advanced approach – vector PFM – based on combination of VPFM and LPFM has been developed.

3. Vector PFM

Electromechanical response of the surface to the applied tip bias in general case is a *vector* having three independent components (PR_x, PR_y, PR_z). To obtain complete information on materials properties, all three components are required. The original VPFM approach allowed only the measurement of PR_z component. Lateral PFM allows PR_y component to be detected simultaneously (the cantilever is oriented along the *x*-axis). Combined lateral and vertical PFM imaging had been used by Eng *et al*. to reconstruct surface crystallography in a barium titanate crystal [23]. Rodriguez *et al*. have applied this approach to 3D polarization reconstruction in micrometer-size PZT capacitors [25]. In both cases, sequential acquisition of two LPFM images at two orthogonal orientations of the sample with respect to the cantilever, further referred to as *x*-LPFM and *y*-LPFM imaging, has been accomplished in the samples with well-defined crystallographic orientation. In general case of an arbitrarily oriented sample, only semi-quantitative information on materials properties can be obtained unless relative sensitivities of LPFM and VPFM are carefully calibrated.

An example of 2D vector PFM image is illustrated in Fig. 3, which shows VPFM and LPFM images of a strontium bismuth tantalate (SBT) thin film (Fig. 3a and b,

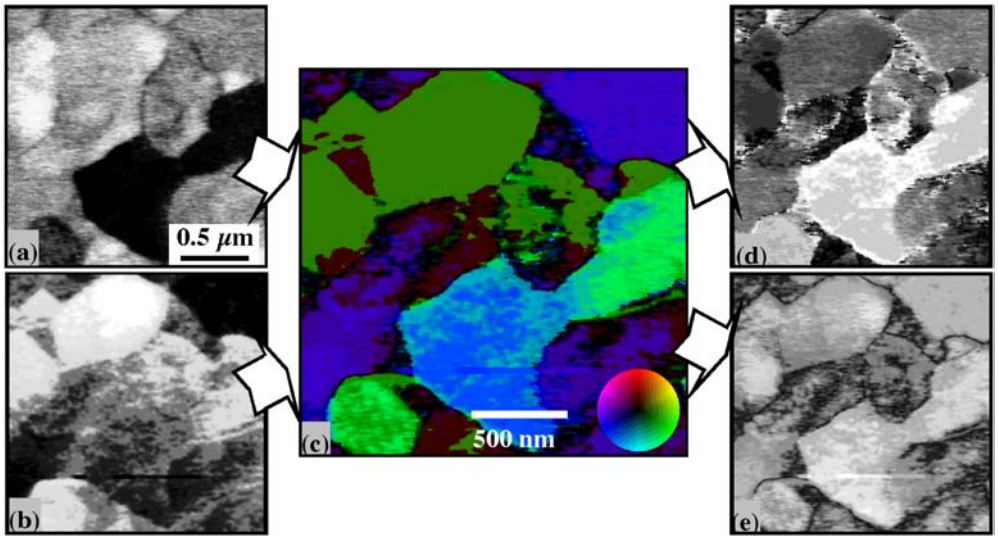

Figure 3 (a) Vertical and (b) lateral PFM images of the SBT thin film. (c) Vector representation of 2D PFM data; (d) Angle and (e) amplitude images derived from image the 2D map in (c).

respectively). To represent vector PFM data, the VPFM and LPFM images are normalized so that the intensity changes between –1 and 1, i.e. vpr, $lpr \in (-1, 1)$. Using commercial software [26] 2D vector data (vpr, lpr) is converted to the amplitude/angle pair, $A_{2D} = \mathrm{Abs}(vpr + I\,lpr)$, $\theta_{2D} = \mathrm{Arg}(vpr + I\,lpr)$. In Fig. 3c, color corresponds to the orientation, while intensity corresponds to the magnitude. Notably, this vector PFM image shows that color is virtually uniform inside most of the grains, suggesting that they exist in a single domain state, while polarization orientation changes between the grains. This information can be represented in the scalar form by plotting separately phase θ_{2D}, and magnitude, A_{2D}, as illustrated in Fig. 3d and e, respectively.

To achieve the full potential of vector PFM, quantitative interpretation of the electromechanical response data is required. The units of PFM response are (nm/V), similar to the dimensionality of piezoelectric constant tensor, d_{ij}. In the uniform z-oriented electric field, response in z-direction is given by the piezoelectric constant d_{33}. In LPFM, under similar conditions the signal is given by the shear components of piezoelectric constant tensor, $xPR_l = d_{35}$ and $yPR_l = d_{34}$, since components d_{31} and d_{32} result in axially symmetric deformation of material that does not contribute to displacement at the center [27]. For the non-uniform field similar to that below the SPM tip, this approximation is no longer rigorous and the effective piezocoefficient will be a complex function of mechanical and electromechnical constants of material. Although the exact analytical solutions are not available for these cases, following the analogy with VPFM, the assumption $xPR_l = d_{35}$ and $yPR_l = d_{34}$ are expected to provide a good first approximation for the description of the LPFM data, even though analytical solutions or numerical simulations are required to prove this conjecture.

Note that this interpretation applies when the piezoelectric tensor is given in the laboratory coordinate system. However, it is conventional to represent the piezoelectric constant tensor in the coordinate system related to the orientation of crystallographic axis of the material, d^0_{ij}. In this case, the intrinsic material symmetry limits the number of non-zero components and allows the material-specific parameters to be tabulated. These coordinate systems are related by three Euler rotation angles, ϕ, θ, and ψ. The relationship between the d_{ij} tensor in the laboratory coordinate system and the d^0_{ij} tensor in the crystal coordinate system is [28]:

$$d_{ij} = A_{ik} d^o_{kl} N_{lj} \tag{7}$$

where the elements of the rotation matrices N_{ij} and A_{ij} as a function of Euler angles are given in Ref. [28]. For example, for a domain in tetragonal ferroelectric material with polarization in the (010) direction oriented perpendicular to the cantilever axis, the relationship between coordinate systems is given by $\phi = 0$, $\theta = \pi/2$, $\psi = 0$ and from Equation 7 $vPR = 0$, $xPR_l = d^0_{15}$ and $yPR_l = 0$, consistent with the early assumption of $xPR_l = d^0_{15}$ for in-plane domains in tetragonal ferroelectrics [24].

To summarize, Equation 7 fully describes the relationship between material properties and vector PFM data and allows semi-quantitative assessment of d^0_{ij} provided that the crystallographic orientation of the sample is known. Alternatively, if the elements of the d^0_{ij} tensor are known then reconstruction of local crystallographic orientation from vector PFM data can be performed.

4. Electromechanics of ferroelectric switching in PFM

Scanning force microscopy provides a unique opportunity for controlling the ferroelectric properties at the nanoscale

and direct studies of the domain structure evolution under an external electric field, which cannot be matched by previously available techniques. A conductive probing tip can be used not only for domain visualization but also for modification of the initial domain structure. Application of a small dc voltage between the tip and bottom electrode generates an electric field of several hundred kilovolts per centimeter, which is higher than the coercive voltage of most of ferroelectrics, thus inducing local polarization reversal. This approach was suggested for such applications as ultrahigh density data storage [6, 7] and ferroelectric lithography [8, 9]. These applications require thorough understanding of both thermodynamics and kinetics of the switching process as described in the following two sections.

The driving force for the 180° polarization switching process in ferroelectrics is change in the bulk free energy density [29, 30]:

$$\Delta g_{\text{bulk}} = -\Delta P_i E_i - \Delta d_{i\mu} E_i X_\mu \tag{8}$$

where P_i, E_i, X_μ, and $d_{i\mu}$, are components of the polarization, electric field, stress and piezoelectric constants tensor, correspondingly, $i = 1, 2, 3$, and $\mu = 1, .., 6$. The first and second terms in Equation 8 describe ferroelectric and ferroelectroelastic switching, respectively. For materials, such as $LiNbO_3$ and lead zirconate-titanate (PZT), the signs of the corresponding free energy terms are opposite and the polarities of the domains formed by ferroelectric and ferroelectroelastic switching are opposite, thus providing an approach to distinguish these switching mechanisms.

The free energy of the nucleating domain is

$$\Delta G = \Delta G_{\text{bulk}} + \Delta G_{\text{wall}} + \Delta G_{\text{dep}} \tag{9}$$

where the first term is the change in bulk free energy, $\Delta G_{\text{bulk}} = \int \Delta g_{\text{bulk}} dV$, the second term is the domain wall energy, and the third term is the depolarization field energy. In the Landauer model of switching, the domain shape is approximated as a half ellipsoid with the small and large axis equal to r_d and l_d, correspondingly (Fig. 4a). The domain wall contribution to the free energy in this geometry is $\Delta G_{\text{wall}} = b r_d l_d$, where $b = \sigma_{\text{wall}} \pi^2/2$ and σ_{wall} is the direction-independent domain wall energy. The depolarization energy contribution is $\Delta G_{\text{dep}} = c r_d^4/l_d$, where

$$c = \frac{4\pi P_s^2}{3\varepsilon_{11}} \left[\ln\left(\frac{2 l_d}{r_d} \sqrt{\frac{\varepsilon_{11}}{\varepsilon_{33}}} \right) - 1 \right] \tag{10}$$

has only a weak dependence on the domain geometry [31].

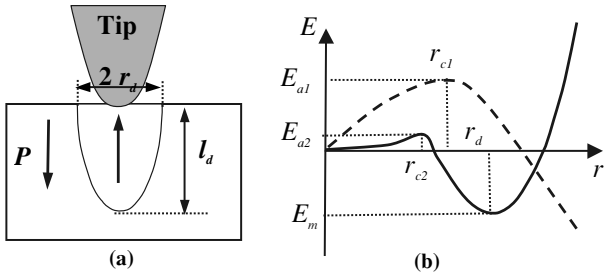

Figure 4 (a) Domain geometry during tip-induced switching. (b) Free energy as a function of the lateral domain size. Dashed line - in a uniform electric field; Solid line – in a tip-induced electric field.

In the uniform field case, the free energy surfaces as a function of l_d, r_d, has a saddle point character and the domain grows indefinitely once the critical size corresponding to activation barrier for nucleation E_a is reached (Fig. 4b). The critical domain size and activation energy for nucleation can be obtained from minimization of Equation 10 as $r_c = 0.83\, b/a$, $l_c = 1.86\, bc^{1/2}\, a^{-3/2}$ and $E_a = 0.518\, b^3 c^{1/2}\, a^{-5/2}$, where $a = 4\pi P_s E/3$. For typical ferroelectric materials, such as $BaTiO_3$ ($\sigma = 7$ mJ/m^2, $P_s = 0.26$ C/m^2, $\varepsilon_{11} = 2000$, $\varepsilon_{33} = 120$ [32]), in the uniform field $E = 10^5$ V/m the corresponding values are $E_a = 2.4 \times 10^5$ eV and $l_c = 16.4$ μm, $r_c = 0.264$ μm. Thus, for relatively weak fields corresponding to experimental coercive fields, homogeneous domain nucleation is impossible, which explains why in typical ferroelectric materials domain nucleation occurs at the surface or at the interface defects.

The opposite is true for the tip-induced switching, when the small radius of curvature of the tip results in large (10^6–10^9 V/m) electric fields localized at the tip apex. The corresponding domain free energy can be determined from electroelastic field distribution generated by the PFM tip as

$$\begin{aligned} \Delta G_{\text{bulk}} &= \int_V \Delta g_{\text{bulk}}(\vec{r}) dV \\ &= 2\pi \int_0^{l_d} dz \int_0^{r(z)} \Delta g_{\text{bulk}}(r, z)\, r\, dr \end{aligned} \tag{11}$$

where $r(z) = r_d \sqrt{1 - z^2/l_d^2}$. An initial insight into the PFM switching phenomena can be obtained using point charge models that are applicable if domain sizes l_d, $r_d \gg R$, a, where R is the tip radius and a is the contact radius and provided that the singularity at the origin is weak enough to ensure convergence of the integral in Equation 11. For ferroelectric switching induced by a point charge q_s located on the surface, the integral in Equation 11 can be taken analytically: $\Delta G_{\text{bulk}} = d r_d l_d/(l_d + \gamma r_d)$, where $d = 2P_s q_s/(\varepsilon_0 + \sqrt{\varepsilon_{11}\varepsilon_{33}})$ and $\gamma = \sqrt{\varepsilon_{33}/\varepsilon_{11}}$. In this point charge approximation, domain size and energy are $r_e = 0.342 d^{2/3} (bc)^{-1/3}$, $l_e = 0.2 d/b$ and $E_m = -0.205 d^{5/3} (bc)^{-1/3}$ [33, 34].

The activation energy for domain nucleation in this approximation is zero, due to the infinite field at the origin. This analysis predicts that domain shape in the switching process follows the invariant relation $r_e^3/l_e^2 = b/c$.

The applicability of the point charge approximation to the thermodynamics of domain switching on the large length scales is limited by the contribution of the electrostatic fields produced by the conical part of the tip, which decay much slower than that produced by the point charge. At the smaller length scales comparable to the tip radius of curvature, the thermodynamics of switching process requires exact electroelastic field structure to be taken into account. In this case, it was shown that domain nucleation requires certain threshold bias of the order of 0.1–1 V, corresponding to non-zero activation energy for nucleation (of the order of $\sim kT$) [29, 35].

In the last several years, a number of reports have become available on the high-order ferroic switching in PFM [30, 35]. Due to the rapid decay of corresponding electroelastic fields, the use of Equation 11 in the point charge/force approximation results in singularity in the contact area, necessitating exact electroelastic field structure to be taken into account. Using rigorous electroelastic solutions, it was shown [35] that for higher order ferroic switching (e.g. ferroelectroelastic), the domain size is limited by the tip-sample contact area, thus allowing precise control of domain size. Finally, the non-linear effects could have severe impact in PFM and should be taken into account at high frequencies [36].

5. PFM spectroscopy

One of the most important applications of PFM is local piezoelectric spectroscopy, i.e., measurements of local hysteresis loops at the ~10 nm level [24, 37]. PFM hysteresis loops readily provide information on local electromechanical activity and coercive voltage variations between dissimilar grains. Currently, there are two main approaches to the hysteresis loop measurements in PFM that differ by the mode of voltage application: either step voltage or pulse voltage. Depending on the dielectric properties of the ferroelectric sample and domain stability one or another approach provides more reliable results [38]. However, generally quantitative interpretation of PFM spectroscopy presents a complex problem. As has been discussed previously, a major challenge of quantitative PFM characterization of ferroelectric thin films stems from the inhomogeneous distribution of the tip-generated field and random grain orientation [39, 40]. The vector PFM approach in conjunction with the local switching experiments can be used to analyze the effect of grain crystallographic orientation on the local hysteresis loop parameters [41]. Below, the inhomogeneous distribution of the SPM tip-generated field has been taken into account to quantify the piezoresponse signal of individual grains using the step mode of hysteresis loop measurement.

Fig. 5 shows surface topography along with the VPFM and LPFM images of the strontium bismuth tantalate (SBT) film [42]. Local piezoelectric hysteresis loop measurements [21] show that grains that exhibit strong VPFM contrast also have distinctive hysteresis loops (Fig. 6a), indicative of a large out-of-plane polarization component. On the other hand, the VPFM hysteresis loop for grain 3, which exhibits gray contrast in VPFM, is linear, indicative of non-ferroelectric nature of the grain or purely in-plane polarization corresponding to (001) grain orientation [43]. The LPFM loop of the same grain, shown in Fig. 6b, exhibits clear hysteresis behavior, which is consistent with the in-plane orientation of the polarization vector.

To analyze the hysteresis loop shape in PFM, the vertical surface displacement under the applied tip bias can be calculated as [41, 44]:

$$-\tilde{A}_{\text{piezo}} = \alpha \int_0^\infty d_{33} E_z dz = \alpha d_{33} \left\{ \int_0^l E_z dz - \int_l^\infty E_z dz \right\} \tag{12}$$

where l is the growing domain length. Integration yields $A_{\text{piezo}} = \alpha d_{33}\{V(0) - 2V(l)\}$, where $V(0)$ is the potential on the surface and V(l) is the potential at the domain boundary. It is shown in Ref. [18] that in the strong indentation regime, for distance l from the center of the contact area larger than contact radius a, the potential distribution inside the material can be approximated using

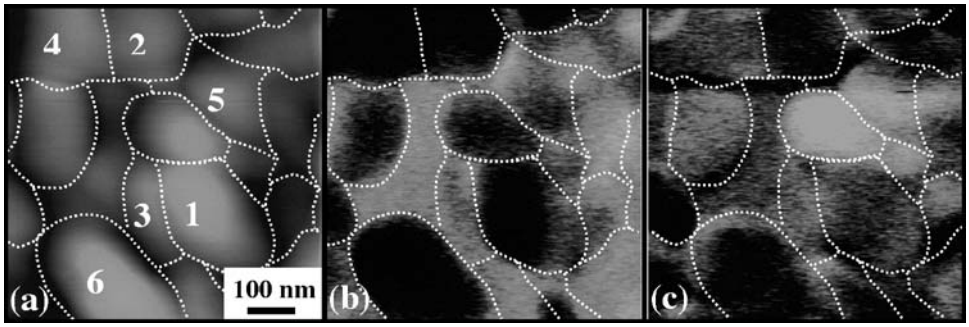

Figure 5 Surface topography (a), vertical (b), and lateral (c) PFM signal of SBT thin film. *Z*-scale in (a) is 20 nm. (Reprinted with permission from [41]).

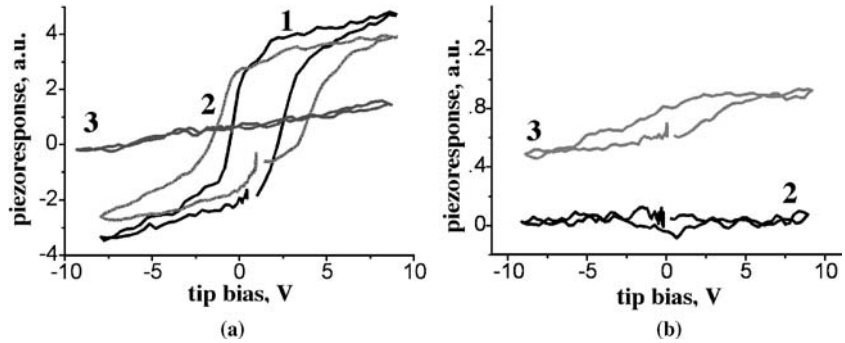

Figure 6 (a) VPFM and (b) LPFM piezoelectric hysteresis loops for grains in Fig. 5. For clarity, vertical loops are shown only for grains 1, 2, and 3. (Reprinted with permission from [41]).

the point-charge model. In this case, assuming that in the point-charge approximation the domain size is related to the biasing voltage as $l(V_{dc}) \sim V_{dc}$ [33, 34], it can be shown that the shape of the PFM hysteresis loop should follow the functional form

$$PR = \alpha d_{33}\{1 - \eta/V_{dc}\} \tag{13}$$

where PR is the piezoresponse amplitude, $PR = A_{piezo}/V_{ac}$. To compare the experimental PFM loop shape with Equation 13, adjustment for the capacitive cantilever-surface interaction is introduced by subtracting the linear loop for the grain 3 from the hysteresis loops for the ferroelectric grains. A corrected hysteresis loop and a corresponding fit by Equation 13 are shown in Fig. 7a, illustrating excellent agreement of the experimental data with Equation 13. Generally, however, care should be taken while subtracting the linear contribution of the cantilever-surface interaction as it might differ for differently oriented grains. This is particularly important for materials with high anisotropy of the dielectric constants, such as barium titanate.

The same formalism has been extended to determine the effect of grain orientation on local coercive voltage. The longitudinal piezoelectric coefficient in SBT in the [011] plane at the angle θ from the (010) axis can be estimated as $d_{zz}(\theta) \approx d_{33} \cos^3 \theta$. Similarly, the lateral piezoresponse coefficient is $d_{zx}(\theta) = d_{31} \cos\theta$. Both vertical and lateral responses decrease with the deviation from the polar (010) direction. The relationship between the PFM coercive bias and crystallographic orientation of the grain can be estimated from the work of switching, which is proportional to $\mathbf{E} \cdot \mathbf{P} = E\,P \cos(\theta)$, where $\mathbf{E}$ is electric field and $\mathbf{P}$ polarization vector. Therefore, coercive bias is expected to increase with deviation angle from polar axis as $V_{coer}(0)/\cos(\theta)$, where $V_{coer}(0)$ is coercive bias for the (010) grain. Comparison of the angular dependence of piezoresponse signal and coercive bias suggests that for the off-axis orientation of the grains the response decreases and coercive bias increases, in agreement with experimental results illustrated in Fig. 7b. In the limiting case of the (001)-oriented grain in SBT piezoresponse and a coercive field become zero and infinity, respectively. It is worthwhile mentioning that establishing correlation between local and macroscopic coercive voltages requires statistical approach that involves local spectroscopy of a number of grains as well as careful studies of switching behavior of the macroscopic capacitor that incorporates these grains - mission still to be accomplished.

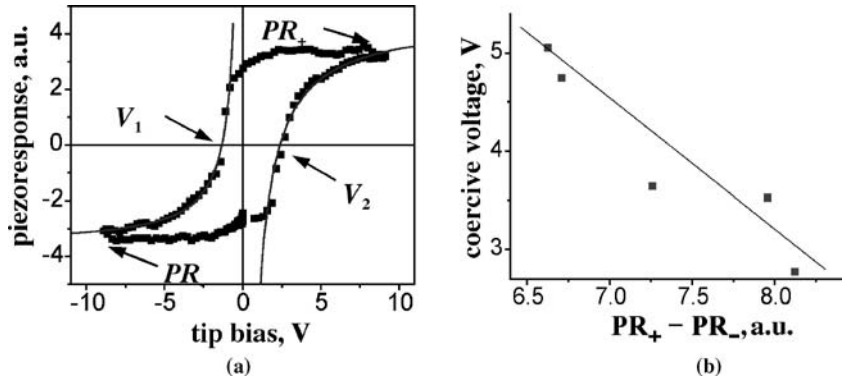

Figure 7 (a) Corrected hysteresis loop and corresponding fit by Equation 13 for positive and negative tip biases. (b) Correlation between maximal switchable polarization and coercive voltage $V_1 + V_2$. (Reprinted with permission from [41]).

6. Domain growth kinetics in PFM

Analysis in Section 4 describes the equilibrium domain shape governed by the extent of electroelastic field created by the tip. However, well outside of the tip-sample contact area, the domain shape and size are controlled by the kinetic effects as discussed below.

When an electric field is applied opposite to the polarization direction of a single-domain ferroelectric capacitor, the switching mechanism involves several steps: nucleation of multiple domains, their forward growth, subsequent sideways expansion and coalescence [45]. In PFM, switching involves nucleation of a single domain as was discussed in the previous sections. High spatial resolution of the PFM approach allows direct investigation of the nanoscale domain growth. However, poor time resolution, which is determined by the time required for image acquisition (∼several minutes) makes *in situ* measurements of domain dynamics during fast switching processes difficult. While PFM can be readily used to investigate slow polarization relaxation processes with characteristic times of the order of minutes and above, it is a challenge to deduce the mechanism of domain transformation when polarization reversal occurs in a matter of microseconds and faster.

This problem is usually circumvented by studying the domain structure dynamics in a quasi-static regime using *step-by-step switching*. This method has been previously used at the macroscopic level in classical switching experiments on correlating the domain structure evolution and transient current in ferroelectric crystals [45] and later was applied to thin films [6, 46]. In this approach, partial reversal of polarization is generated by applying a voltage pulse shorter than the total switching time with subsequent piezoresponse imaging of the resulting domain pattern. By applying a sequence of voltage pulses of successively increasing duration and acquiring piezoresponse images after each pulse a consistent picture of time dependent behavior of domain structure can be obtained providing information on the domain wall velocity, its spatial anisotropy and its field dependence. To avoid data misinterpretation due to spontaneous backswitching between the pulses, stability of the produced intermediate patterns should be checked by acquiring domain images at different time intervals after single pulse application. To describe the sidewise expansion of the domain it is necessary to take into account the field dependence of the domain wall velocity and the spatial distribution of the electric field generated by the probing tip.

Fig. 8 shows the PFM amplitude and phase images of an array of 9 domains fabricated in a lithium niobate crystal by applying negative 10 ms voltage pulses of various magnitudes in the range from 20 to 70 V [47]. The PFM contrast is the same across the 180° domain boundaries, which appear as dark lines in the amplitude image, suggesting that the fabricated domains extend from the top to the bottom interface. Fig. 9 shows the time dependence of the domain radius for three different pulse amplitudes, which follows logarithmic law [48]. In addition, it has been found that the domain size follows linear voltage dependence [49]. This behavior suggests that the domains in Fig. 8 represent different stages of the switching kinetic process and do not correspond to the equilibrium state domains [33]. Notably, results shown in Fig. 8 suggest that the kinetics of the sidewise domain growth can be described by a universal scaling curve $g(t) = r(V, t)/V$ illustrated in inset in Fig. 9. It is suggested that this universal scaling behavior is directly related to the field dependence of domain wall velocity and field distribution inside the material. Here, we analyze the kinetics of the sidewise domain growth using the classical activation model of the wall motion in the tip-generated field assuming a weak indentation regime [50].

To calculate the tip-generated field distribution, the tip was modeled as a charged sphere with radius R at the distance δ from the sample surface. The normal component of this electric field at a section of the 180° domain wall with the sample surface at a distance r from the tip

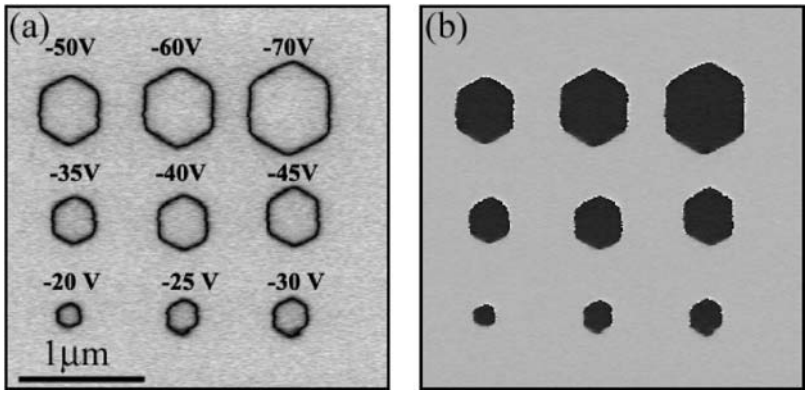

Figure 8 VPFM (a) amplitude and (b) phase images of ferroelectric domains fabricated in lithium niobate by 10 ms voltage pulses of various amplitudes. (Reprinted with permission from [47]).

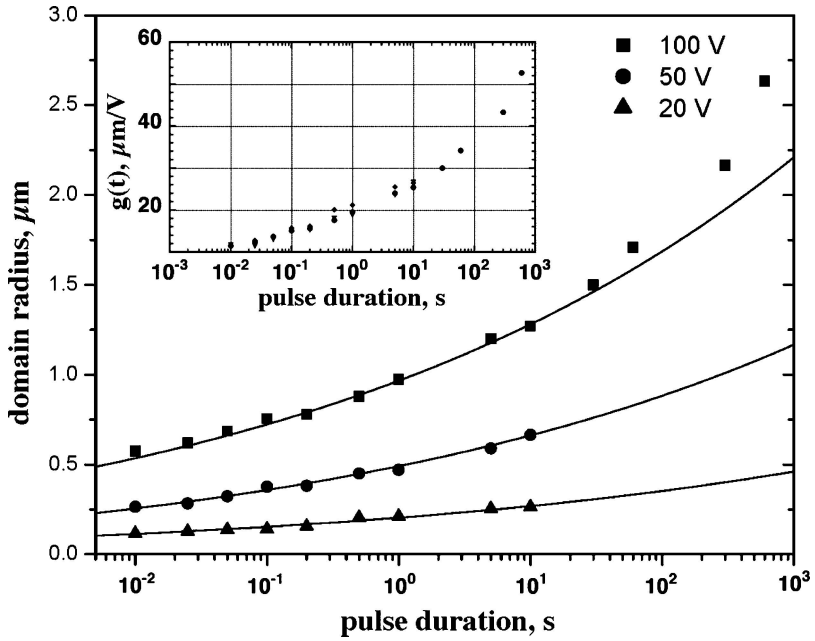

Figure 9 Domain radius versus the pulse duration for various pulse magnitudes lithium niobate. Inset shows a scaling curve $g(t) = r(V, t)/V$ calculated using all data points from the main plot in Fig. 9. (Reprinted with permission from [47]).

is calculated using an expression for the electric potential from Mele [51]:

$$E(r) = \frac{C_t V_t}{2\pi\varepsilon_0\sqrt{\varepsilon_c\varepsilon_a} + 1}\sqrt{\frac{\varepsilon_a}{\varepsilon_c}}\frac{R+\delta}{((R+\delta)^2 + r^2)^{3/2}} \quad (14)$$

where C_t and V_t are the tip capacitance and bias, respectively, and ε_a and ε_c are the dielectric constants along the non-polar and polar axes of the sample, respectively. In the present study, we used the following values: $R = 50$ nm, $\delta = 1$ nm, $\varepsilon_a = 85$, $\varepsilon_c = 30$. The tip capacitance was calculated to be 1.6×10^{-17} F [47]. The set of data in Fig. 9 has been fitted using the following expression for the time dependence of the domain radius assuming an exponential field dependence of the wall velocity [52]:

$$t = \int \frac{dr}{v(r)} = \int \frac{dr}{e^{-\alpha/E(r+r_0)}} \quad (15)$$

where v (r) is a local wall velocity and α is the activation field. The meaning of the fitting parameter r_0 can be understood as follows. Underneath the probing tip, the generated field is much larger than the local coercive field and the domain growth develops as a nonactivated process. The spatial inhomogeneity of the tip-generated field results in a transition from the nonactivated to the activated process. Therefore, r_0 can be considered as the domain radius at which the activation type of the wall motion begins. The r_0 value was found to be 17 nm for the applied voltage of 20 V and 110 nm for the 100 V voltage. The activation energy was found to decrease with an increase in the applied voltage from $\sim 2\times10^3$ kV/cm for 20 V to $\sim$50 kV/cm for 100 V. It should be noted that a strong decrease of the external field with the distance from the tip as well as non-local tip effect might result in a different mechanism of domain wall motion that may explain a less adequate fitting of $r(t)$ for large ($r > 1.5$ μm) domains in Fig. 9.

7. Conclusion

Rapid development of ferroelectric-based devices generated a strong need for extensive investigation of the nanoscale properties of ferroelectric materials. Application of piezoresponse force microscopy to ferroelectrics opened new possibilities not only for their high-resolution imaging of domain structures, but also for quantitative characterization and control of ferroelectric properties at the nanoscale. Clearly, future will evidence broad application of this technique for ferroelectrics, as well as for more broad class of piezoelectric and electrostrictive materials. It is also expected that PFM will find wide application in studying the electromechanical coupling in biological materials that will open new horizons for understanding the mechanisms that govern growth and regeneration of living tissues.

Acknowledgments

AG acknowledges financial support of the National Science Foundation (Grant No. DMR02-35632). Research performed in part as a Eugene P. Wigner Fellow and staff member at the Oak Ridge National Laboratory, managed

by UT-Battelle, LLC, for the U.S. Department of Energy under Contract DE-AC05-00OR22725 (SVK). Support from ORNL SEED funding is acknowledged (SVK).

References

1. D. SARID, Scanning Force Microscopy with Applications to Electric, Magnetic and Atomic Forces, Oxford Series in Optical and Imaging Sciences (University Press, Oxford, 1991).
2. R. WIESENDANGER, Scanning Probe Microscopy and Spectroscopy: Methods and Applications (University Press, Cambridge, 1994).
3. D. A. BONNELL, Scanning Probe Microscopy and Spectroscopy: Theory, Techniques, and Applications (John Wiley & Sons, October 2000).
4. V. TSUKRUK, Advances in Scanning Probe Microscopy (Macromolecular Symposia 167), (John Wiley & Sons, July 2001).
5. A. DE STEFANIS and A. A. G. TOMLINSON, Scanning Probe Microscopies: From Surfaces Structure to Nano-Scale Engineering, Trans Tech Publications, Ltd.; April 2001.
6. T. TYBELL, P. PARUCH, T. GIAMARCHI and J.-M. TRISCONE, *Phys. Rev. Lett.* **89** (2002) 097601.
7. K. TERABE, M. NAKAMURA, S. TAKEKAWA, K. KITAMURA, S. HIGUCHI, Y. GOTOH and Y. CHO, *Appl. Phys. Lett.* **82** (2003) 433.
8. S. V. KALININ, D. A. BONNELL, T. ALVAREZ, X. LEI, Z. HU, J. H. FERRIS, Q. ZHANG and S. DUNN, *Nano Letters* **2** (2002) 589.
9. S. V. KALININ, D. A. BONNELL, T. ALVAREZ, X. LEI, Z. HU, R. SHAO and J. H. FERRIS, *Adv. Mat.* **16** (2004) 795.
10. See, for example, references in A. Gruverman, in "Encyclopedia of Nanoscience and Nanotechnology", edited by H.S.Nalwa, (American Scientific Publishers, Los Angeles, Vol. 3, 2004) pp. 359–375.
11. W. G. CADY, Piezoelectricity: An Introduction to the Theory and Applications of Electromechanical Phenomena in Crystals (Dover Publications, New York, 1964).
12. A. F. DEVONSHIRE, *Philos. Mag.* **40** (1949) 1040.
13. A. F. DEVONSHIRE, *Adv. Phys.* **3** (1954) 85.
14. P. GUTHNER and K. DRANSFELD, *Appl. Phys. Lett.* **61** (1992) 1137.
15. K. FRANKE, J. BESOLD, W. HAESSLE and C. SEEGEBARTH, *Surf. Sci. Lett.* **302** (1994) L283.
16. A. GRUVERMAN, H. TOKUMOTO, S. A. PRAKASH, S. AGGARWAL, B. YANG, M. WUTTIG, R. RAMESH, O. AUCIELLO and V. VENKATESAN, *Appl. Phys. Lett.* **71** (1997) 3492.
17. T. HIDAKA, T. MARUYAMA, M. SAITOH, N. MIKOSHIBA, M. SHIMIZU, T. SHIOSAKI, L. A. WILLS, R. HISKES, S. A. DICAROLIS and J. AMANO, *Appl. Phys. Lett.* **68** (1996) 2358.
18. S. V. KALININ, E. KARAPETIAN and M. KACHANOV, *Phys. Rev. B* **70** (2004) 184101.
19. E. KARAPETIAN, M. KACHANOV and S. V. KALININ, *Phil. Mag.*, in print
20. S. V. KALININ and D. A. BONNELL, *Phys. Rev.* **B 65** (2002) 125408.
21. Nanoscale Characterization of Ferroelectric Materials, edited by M. Alexe and A. Gruverman (Springer-Verlag, Berlin, 2004).
22. L. M. ENG, H.-J. GÜNTHERODT, G. ROSENMAN, A. SKLIAR, M. ORON, M. KATZ and D. EGER, *J. Appl. Phys.* **83** (1998) 5973.
23. L. M. ENG, H.-J. GUNTHERODT, G. A. SCHNEIDER, U. KOPKE and J. M. SALDANA, *Appl. Phys. Lett.* **74** (1999) 233.
24. A. ROELOFS, U. BÖTTGER, R. WASER, F. SCHLAPHOF, S. TROGISCH and L. M. ENG, *Appl. Phys. Lett.* **77** (2000) 3444.
25. B. J. RODRIGUEZ, A. GRUVERMAN, A. I. KINGON, R. J. NEMANICH and J. S. CROSS, *J. Appl. Phys.* **95** (2004) 1958.
26. Mathematika 5.0, Wolfram Research.
27. S. V. KALININ, B. J. RODRIGUEZ, S. JESSE, J. SHIN, A.P. BADDORF, P. GUPTA, H. JAIN, D.B. WILLIAMS and A. GRUVERMAN, unpublished.
28. R. E. NEWNHAM, Properties of Materials: Anisotropy, Symmetry, Structure (Oxford University Press, 2005).
29. M. ABPLANALP, PhD thesis, Swiss Federal Institute of Technology, Zurich (2001).
30. M. ABPLANALP, J. FOUSEK and P. GUNTER, *Phys. Rev. Lett.* **86** (2001) 5799.
31. Equation 10 is valid only for $l_d > r_d$. To avoid this limitation, used here was the expression for the demagnetization factor for prolate ellipsoid from J. A. OSBORN, *Phys. Rev.* **67** (1945) 351.
32. F. JONA and G. SHIRANE, Ferroelectric Crystals, (Dover Publications, New York, 1993).
33. M. MOLOTSKII, *J. Appl. Phys.* **93** (2003) 6234.
34. M. MOLOTSKII, A. AGRONIN, P. URENSKI, M. SHVEBELMAN, G. ROSENMAN and Y. ROSENWAKS, *Phys. Rev. Lett.* **90** (2003) 107601.
35. S. V. KALININ, A. GRUVERMAN, B. J. RODRIGUEZ, J. SHIN, A. P. BADDORF, E. KARAPETIAN and M. KACHANOV, *J. Appl. Phys.* **97**, 074305 (2005).
36. B. D. HUEY, in "Nanoscale Phenomena in Ferroelectric Thin Films," edited by S. Hong (Kluwer Academic Publishers, 2004).
37. M. ALEXE, A. GRUVERMAN, C. HARNAGEA, N. D. ZAKHAROV, A. PIGNOLET, D. HESSE and J. F. SCOTT, *Appl. Phys. Lett.* **75** (1999) 1158.
38. S. HONG, J. WOO, H. SHIN, J. U. JEON, Y. E. PAK, E. L. COLLA, N. SETTER, E. KIM and K. NO, *J. Appl. Phys.* **89** (2001) 1377.
39. C. HARNAGEA, A. PIGNOLET, M. ALEXE and D. HESSE, *Integrated Ferroelectrics* **38** (2001) 23.
40. C. HARNAGEA, PhD thesis, Martin-Luther-Universität Halle Wittenberg, Halle, 2001.
41. S. V. KALININ, A. GRUVERMAN and D. A. BONNELL, *Appl. Phys. Lett.* **85** (2004) 795.
42. Shown here are PFM images representing the $A \cos \theta$ signal, where A is piezoresponse amplitude and θ is phase.
43. A. GRUVERMAN, A. PIGNOLET, K. M. SATYALAKSHMI, M. ALEXE, N. D. ZAKHAROV and D. HESSE, *Appl. Phys. Lett.* **76** (2000) 106.
44. C. S. GANPULE, V. NAGARJAN, H. LI, A. S. OGALE, D. E. STEINHAUER, S. AGGARWAL, E. WILLIAMS, R. RAMESH and P. DE WOLF, *Appl. Phys. Lett.* **77** (2000) 292.
45. E. FATUZZO and W. J. MERZ, Ferroelectricity (North-Holland, Amsterdam, 1967).
46. O. LOHSE, S. TIEDKE, M. GROSSMANN and R. WASER, *Integrated Ferroelectrics* **22** (1998) 123.
47. B. J. RODRIGUEZ, R. J. NEMANICH, A. KINGON, A. GRUVERMAN, S. V. KALININ, K. TERABE, X. Y. LIU and K. KITAMURA, *Appl. Phys. Lett.* **86** (2005) 012906.
48. A. AGRONIN, Y. ROSENWAKS and G. ROSENMAN, *Appl. Phys. Lett.* **85** (2004) 452.
49. For pulse duration of 10 ms this linear behavior holds at least up to 250 V.
50. S. V. KALININ, A. GRUVERMAN, J. SHIN, A. P. BADDORF, E. KARAPETIAN and M. KACHANOV, cond-mat/0406383.
51. E. J. MELE, *Am. J. Phys.* **69** (2001) 557.
52. R. C. MILLER and G. WEINREICH, *Phys. Rev.* **117** (1960) 1460.